



## Article

# A Non-Invasive Method for Measuring Bubble Column Hydrodynamics Based on an Image Analysis Technique

Neha Agarwal <sup>1</sup>, Moonyong Lee <sup>1,\*</sup>  and Hyunsung Kim <sup>2,\*</sup> <sup>1</sup> School of Chemical Engineering, Yeungnam University, Gyeongsan 38541, Korea<sup>2</sup> School of Computer Science, Kyungil University, Gyeongsan 38424, Korea

\* Correspondence: mynlee@yu.ac.kr (M.L.); kim@kiu.ac.kr (H.K.)

**Abstract:** Bubble size and its distribution are the important parameters which have a direct impact on mass transfer in bubble column reactors. For this, a new robust image processing technique was presented for investigating hydrodynamic aspects and bubble behavior in real chemical or biochemical processes. The experiments were performed in a small-scale bubble column. The study was conducted for the wide range of clear liquid heights and superficial gas velocities. However, a major challenge in image analysis techniques is identification of overlapping or cluster bubbles. This problem can be overcome with the help of the proposed algorithm. In this respect, large numbers of videos were recorded using a high-speed camera. Based on detailed experiments, the gas–liquid dispersion area was divided into different zones. A foam region width was found as inversely proportional to the clear liquid height. An entry region width was found as directly proportional to the clear liquid height. Hydrodynamic parameters, including gas holdup, bubble size distribution, and Sauter mean bubble diameter were evaluated and compared for different operating conditions. The gas holdup was calculated from both height measurement and pixel intensity methods, and it was found to be indirectly proportional to clear liquid height. Bubble sizes affect the bubble column performance; therefore, bubbles are tracked to calculate the bubble size distribution. Experimental results proved that the proposed scheme is robust.



**Citation:** Agarwal, N.; Lee, M.; Kim, H. A Non-Invasive Method for Measuring Bubble Column Hydrodynamics Based on an Image Analysis Technique. *Processes* **2022**, *10*, 1660. <https://doi.org/10.3390/pr10081660>

Received: 25 July 2022

Accepted: 18 August 2022

Published: 21 August 2022

**Publisher's Note:** MDPI stays neutral with regard to jurisdictional claims in published maps and institutional affiliations.



**Copyright:** © 2022 by the authors. Licensee MDPI, Basel, Switzerland. This article is an open access article distributed under the terms and conditions of the Creative Commons Attribution (CC BY) license (<https://creativecommons.org/licenses/by/4.0/>).

**Keywords:** bubble column reactors; bubble size distribution; gas holdup; image processing technique; multiphase system; hydrodynamics; MATLAB

## 1. Introduction

Bubble column reactors are contacting devices in which the gas phase is bubbled through a liquid phase. Bubble columns (BCs) are often encountered as two-phase reactors in various industries such as chemical, biochemical [1], petrochemical, and wastewater treatment industries [1–3], etc. BCs gained attention for the intense mixing of gas and liquid phases, and they have simple and economic construction and operation. To optimize and control various processes, it is important to characterize the bed height. The existence of a foam region at top of the dispersed bed is quite common in a BC.

Wide research is available in the literature regarding fluid dynamic features, i.e., gas holdup and bubble characteristics affecting the performance of BCs. However, there is little literature available related to foam characteristics in BCs. However, foam region width,  $W_f$ , was not estimated, but the Electrical Capacitance Tomography approach was observed as appropriate for the detection of local water fractions [4]. Variation of gas holdup with superficial gas velocity,  $U$ , was reported for foaming systems [5].

Quantitative research was carried out using a pseudo-2D rectangular BC with dimensions 0.05 m and 0.10 m [6]. The void size was in the range of 0.5–8 mm. The  $W_f$  was calculated by pressure estimation at different axial positions. When  $U$  was in the range between 0.006 and 0.44  $\text{ms}^{-1}$ , then  $W_f$  was evaluated according to Equation (1).

$$W_f = 0.433U^{0.73} \quad (1)$$

Correlation (1) predicts that the value of  $W_f$  is enhanced monotonically with  $U$ . The entry region width,  $W_e$ , was calculated using correlations (2) and (3).

$$W_e = 4.8 - 4.8 \log(U), \text{ for } F \leq 0.1 \quad (2)$$

$$W_e = -0.2 - 4.8 \log(U), \text{ for } F \geq 0.1 \quad (3)$$

where feature  $F$  can be expressed according to the following expression,

$$F = \frac{a_a}{a_c} \quad (4)$$

For a perforated plate (PP)-type gas distributor, correlation (3) is appropriate.

An experimental study on foam region showed that  $W_f$  varies according to the physical characteristics of the system, geometrical features, bubble size, temperature,  $T$ , and pressure,  $P$  [7]. The foam region width was estimated by correlation (5), when gas was dispersed through the highly viscous liquids in a BC.

$$W_f = 2905 \left( \frac{d_b}{2} \right) Ca^{-1} \left( \frac{Fr}{Re} \right)^{1.8} \quad (5)$$

The Reynolds number, Froude number, and Capillary number can be defined as follows,

$$Re = \frac{\rho_l \left( \frac{d_b}{2} \right) (U - U_f)}{\mu_l} \quad (6)$$

$$Fr = \frac{(U - U_f)^2}{\left( \frac{g d_b}{2} \right)} \quad (7)$$

$$Ca = \frac{\mu_l (U - U_f)}{\sigma_l} \quad (8)$$

$U_f$  can be calibrated by extrapolating values for the foam region width with  $U$  and applied in correlations (6) to (8).

Image analysis of bubbles' geometry and their path is accounted for as a direct but time-consuming process, which motivates many researchers to employ efficient non-intrusive image processing (IP) techniques for estimating hydrodynamic features [8] of BC reactors. Commonly used non-intrusive IP techniques presented in state-of-art literature are given as follows:

1. Bubble segmentation and reconstruction method [9].
2. Watershed segmentation technique [10,11].
3. Technique combining geometrical, optical, and topological operations [12].
4. Recursive technique [13].

The above-mentioned algorithms have been employed to analyze fast bubbling flow videos. The bubble geometry, its vertical velocity, flow regime transition, and qualitative characteristics, etc. are a few fluid dynamic features investigated in the state-of-art literature.

The bubble geometry and its path were computed with a fast camera applying the IP technique. A recursive technique was proposed for concave point tracking. This technique was evaluated for gas holdup less than 0.056 [13]. The shape of bubbles deflects from being a perfect sphere in a bubble column. Therefore, the bubble shape is an important parameter to evaluate. The bubble continuously deviates its geometry while traveling in the gas-liquid dispersion area within the reactor. The shapes of bubbles can be defined according to their aspect ratio, AR, which computes the degree of divergence from a perfect sphere. Some of the correlations available in literature for the estimation of bubble diameter under different operating conditions are presented in Table 1.

Recently, many researchers implemented different non-intrusive IP methods for the study of these features in a BC [14] since non-intrusive IP techniques are highly efficient to extract the required information. Fluid dynamics in a small rectangular BC were investigated with the help of recording videos at the frequency of 500 fps for different  $U$  (0.0005–0.004 ms<sup>-1</sup>) [15,16].

**Table 1.** Correlations for bubble diameter,  $d_{32}$ , in bubble columns.

Investigator	Correlation	Remarks
[17]	$\frac{d_{32}}{D} = 26Bo^{-0.5}Ga^{-0.12}Fr^{-0.12}$	$d_{32}$ dec. with inc. in $D$
[18]	For $1 < Re < 10$ $d_{32} = 1.56 \left( Re^{0.058} \left( \frac{\sigma d_o^2}{\Delta \rho_l g} \right)^{1/4} \right)$ For $10 < Re < 2100$ $d_{32} = 0.32 \left( Re^{0.425} \left( \frac{\sigma d_o^2}{\Delta \rho_l g} \right)^{1/4} \right)$ For $4000 < Re < 70000$ $d_{32} = 100 \left( Re^{0.4} \left( \frac{\sigma d_o^2}{\Delta \rho_l g} \right)^{1/4} \right)$	
[19]	$d_b = \left[ \left( \frac{6d_o\sigma}{\rho_l g} \right)^{4/3} + \left( \frac{81\mu_l Q_o}{\pi g \rho_l} \right) + \left( \frac{135Q_o^2}{4\pi^2 g} \right)^{4/5} \right]^{1/4}$	
[20]	$d_b = \left( \frac{\sigma}{\rho_l} \right)^{0.6} \left( \frac{\mu_l}{\mu_g} \right)^{0.1} (U_o g)^{-0.4}$	
[21]	$d_{32} = 0.289\rho_l^{-0.552}\mu_l^{-0.048}\sigma^{0.442}U^{-0.124}$	
[22]	$\frac{d_b}{d_o} = \left[ \left( \frac{5.0}{Bo_b^{1.08}} \right) + 9.261 \left( \frac{Fr^{0.36}}{Ga^{0.39}} \right) + 2.147Fr^{0.51} \right]^{1/3}$	At high $Q_o$ , $d_b$ inc. with $\mu_l$
[23]	$d_{32} = 1.658 \times 10^{-3}U^{-0.12}$	$d_{32}$ dec. with $U$
[24]	$\frac{d_b}{D} = 3.85 * 10^2 Fr^{0.7} Ga^{-0.2} Bo^{-0.3}$	
[25]	$\frac{d_{32}}{D} = 0.9 \left[ We^{0.95} Re^{0.40} Fr^{0.47} \left( \frac{d_o}{D} \right)^{0.55} \right]^{0.51}$	
[26]	$\frac{d_{32}}{d_s} = 12.5 \left[ We^{-15.87} Re^{13.73} Fr^{9.19} \left( \frac{d_o}{d_s} \right)^{2.77} \right]$	
[27]	$d_i = 2.19 * 10^{-9} d_o Re_{d_o}^{1.46} Eo_{d_o}^{-0.52} d_m = 6.75 * 10^{-6} \frac{\sigma^2}{g \mu_l^2} \left( \frac{D}{n_o \rho_p} \right)^{0.47} Re_{d_i}^{0.34}$	$d_m$ inc. with $Re$ and $n_o$ , and dec. with $\delta_p$
[28]	$\frac{d_{32}}{D} = 0.35 \left[ We^{0.95} Re^{0.40} Fr^{0.47} \left( \frac{d_o}{D} \right)^{0.55} \right]^{0.09}$	$d_{32}$ inc. with $U$ , $d_{32}$ inc. axially from bottom to top

A bubble recognition method was applied for the tracing of individual bubbles. The tracking was carried out by locating the bright spot at the center of the bubble. An IP method was implemented to estimate terminal rise velocity,  $U_t$ , of individual bubbles as well as their swarm in elastic liquids [29].

Another IP method had been presented for calculation of bubble size distribution, BSD, in fast bubbling flows with large diameter range (4 mm to 120 mm) and different hole fractions (0.02–0.7) [30]. The IP method categorizes bubbles into distinct groups according to their shape and diameter. The intensity gradient was observed at the center of every bubble. Therefore, overlapping groups of bubbles were segmented into single bubbles. The suggested method was appropriate to study the bubble behavior of each bubble.

A broad BSD was observed at low  $U$ , whereas, at large  $U$ , the BSD was narrow [31]. On increasing the  $U$ , the BSD moved from small to larger bubble sizes. The variation of bubble diameter is directly proportional to the height. The BSD was not significantly

influenced by the variation of superficial liquid velocity. Increasing both pressure and temperature resulted in the BSD moving from larger to smaller bubble sizes. However, BSD is significantly influenced by liquid-phase properties [28]. At low  $U$ , bubble behavior was highly affected by the experimental facility instead of the operating conditions [16]. When internals are equipped in the reactor, the BSD is wider in comparison with a reactor in the absence of internals [32]. The knowledge of BSD facilitates the estimation of flow regime transition [33]. The convolutional neural network-based method was proposed with high overlapping and gas holdup up to 20%. The experiments were performed with air and different liquids in both 2D and 3D bubble columns [34].

The variation of BSD, AR, and the bubble alignment with  $U$  were investigated in an annular gap BC under a homogeneous flow regime environment. The IP technique had been applied to estimate  $U$  at which a transition from homogeneous to churn turbulent (CT) flow regime took place.

The proposed work mainly focused on the development of an IP algorithm. The algorithm was used to estimate the width of entry region and foam region with the help of an IP method to process video. The algorithm was also built and trained to estimate the gas holdup. Variations of foam region width, entry region width, and gas holdup with  $U$  and clear liquid height,  $H_c$ , were also studied. Another IP technique was also built and trained to recognize the overlapping clusters of bubbles and to estimate the BSD.

## 2. Proposed Scheme

The image analysis technique was applied to detect the bubbles present in different zones. The image analysis algorithm written in MATLAB for measurement of bubble hydrodynamics is presented in Figure 1. The frames from videos captured were extracted and analyzed to evaluate different bubble hydrodynamic parameters. Contour was plotted over original image to verify the correctness of the algorithm. There is a difference in bubble frequency and its size in different zones. Every zone has a different mass transfer and interfacial area. So, it is important to first identify different zones axially. The first zone is the entry zone, i.e., the region near the gas distributor. Next is the fully developed flow zone. Last is the foaming region, where a coalescence and breakup phenomenon takes place. Afterwards, bubble characteristics were calculated in every zone. The effect of  $U$  and  $H_c$  was investigated.

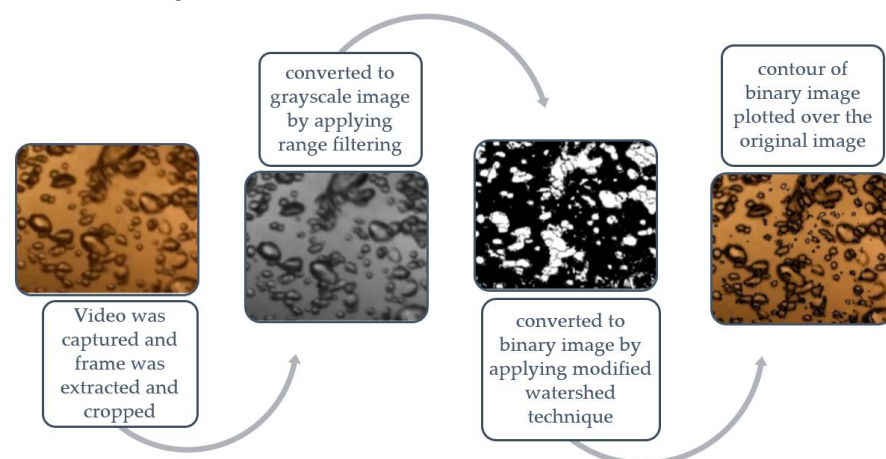


**Figure 1.** Results of the image processing algorithm.

### 2.1. Experimental Setup

The experimental facility was a vertical column of rectangular cross section with dimensions  $0.37\text{ m} \times 0.2\text{ m} \times 0.02\text{ m}$ . A BC is generally constructed of two parts. One part is a bubble generation portion and the second one is the bubble distribution part. The portion of the column below the gas distributor is considered as bubble generation space. Additionally, a portion of the column above the gas distributor is known as the bubble

distribution space. The configuration of the experimental setup is presented in Figure 2. It was constructed of Perspex sheets. To ameliorate the erosion of the reactor wall and provide effortless cleaning, the front and rear walls of the reactor were constructed using glass.

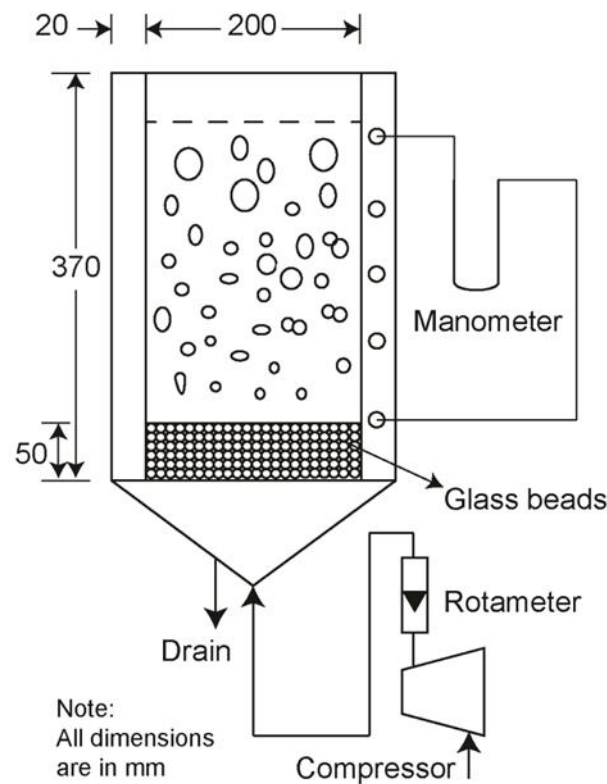


**Figure 2.** Experimental setup.

The gas enters through a sparger so that uniform bubbling takes place. The PP-type gas distributor was used. It consisted of 200 holes. Each hole has a size of 1.5 mm. Above the PP-type gas distributor, glass beads of diameter 5 mm were packed up to a height of 0.05 m. A 200 mesh of stainless steel was assembled over the beads. The section filled with glass beads performs the function of the calming section. The reactor was constructed with a conical bottom below the sparger. Air was introduced through a compressor. A rotameter was used to estimate its flowrate.

Bubbles are difficult to identify because they are transparent and the illumination settings inside the reactor are challenging, which causes the bubble appearance to fluctuate. That is why, for uniform illumination, light sources were equipped at the back of the rear wall. After adjusting the camera location and by providing a proper rear light to the reactor, even lighting in all the images was accomplished. The camera was set to capture videos at the frequency of 120 fps and 400 fps.

## 2.2. Detection of Gas-Liquid Dispersion and Estimation of Bubble Characteristics

Air was introduced into the BC through a gas distributor and was dispersed through water. The camera was turned on to capture videos at the rate of 120 fps. A large number of videos were captured at various  $U$  and  $H_c$ . Experiments were conducted at room temperature and atmospheric pressure. Some bubble clusters were present at large  $U$ .

The videos, once collected, were processed to extract useful information. For this purpose, the IP technique was coded using MATLAB. The video was processed through an IP method as discussed below. The processed images were examined to detect  $W_e$ ,  $W_f$ , and  $H_e$  and the values of these three zones were estimated. As the values of these zones vary rapidly with time, an average of over 60 successive images were used for further calculations. The gas holdup was calculated from the data of expanded gas-liquid

dispersion height. The IP technique applied for the detection of different zones of gas–liquid dispersion is shown in Figure 3.

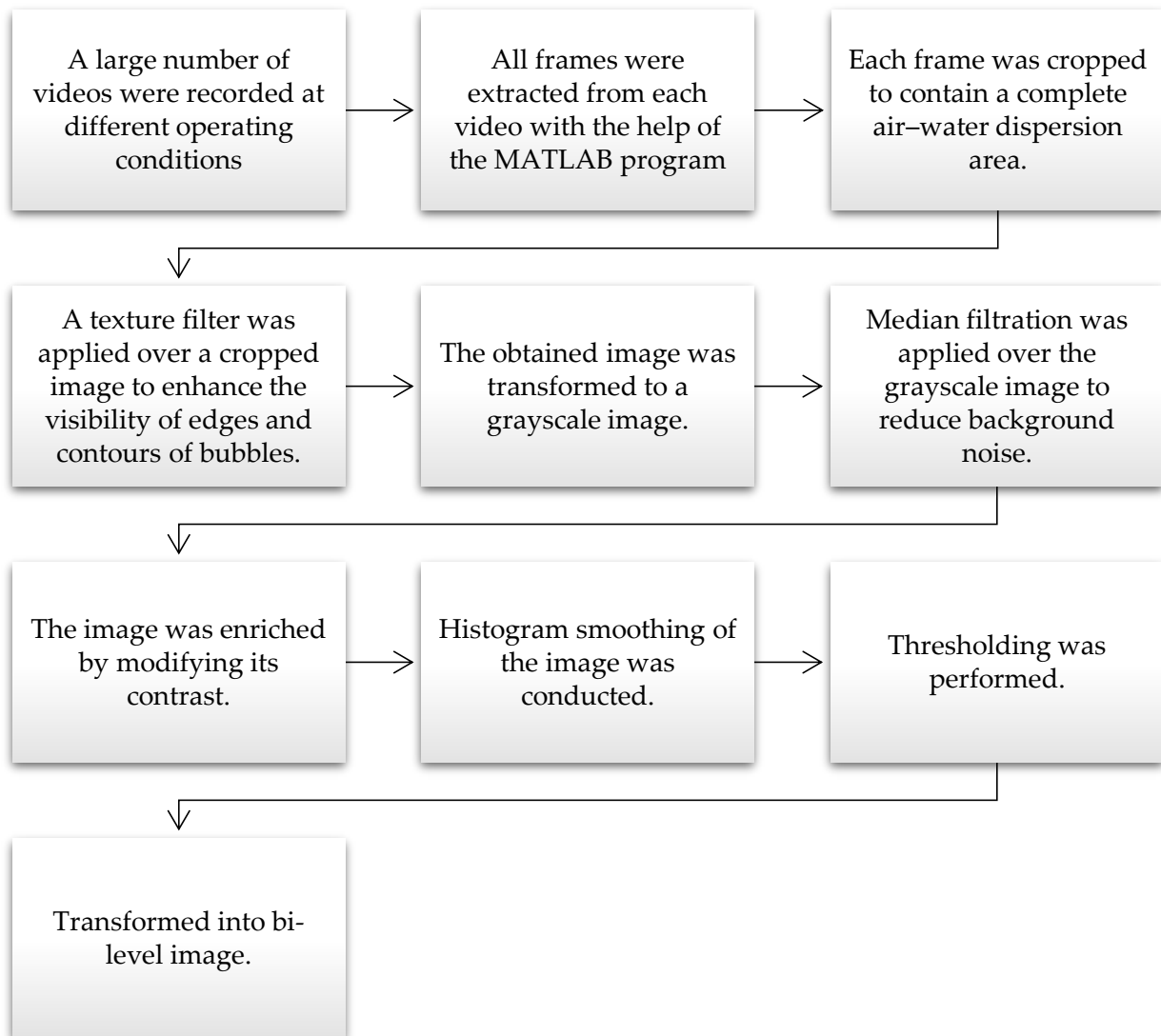


**Figure 3.** Steps for IP algorithm applied for detection of different zones of gas-liquid dispersion.

The *rangefilt* was applied to enhance the visibility of edges and contours of bubbles. The *imadjust* function was used to enrich the contrast. The lowest 1% and the highest 1% of pixel intensities were saturated by the *imadjust* function. For smoothing, the *adapthisteq* function was used. Contrast enhancement limit 0.01 was considered for the *adapthisteq* function. The *graythresh* function was used to calculate the threshold value.

Bi-level images obtained were used to derive information regarding the characteristics of the air–water dispersion in the reactor. In a bi-level image, the white pixel represents bubbles. Black pixels outside the bubbles represent water. Pixel intensity, PI, can be described as follows.

$$PI = \frac{\text{white pixels at particular height above sparger}}{\text{total pixels at particular height above sparger}} \quad (9)$$

The process for the detection of different gas–liquid dispersion zones is completely independent of bubble geometry, but only depends on the IP method developed to achieve phase identification.

After the study of different gas–liquid dispersion zones, the study was carried out to calculate the BSD and the effect of  $U$  and  $H_c$  on BSD. For this purpose, recordings were carried out at a frequency of 400 fps.

Experiments were performed at different  $U$  and various clear liquid heights. The IP technique was coded using MATLAB to examine the recordings. The bi-level image acquired after applying the IP technique was utilized to estimate parameters regarding bubble behavior. The IP algorithm applied for the estimation of bubble characteristics is shown in Figure 4. The frame was extracted and cropped to contain the complete bubbling bed. Then, the cropped frame was converted into a gray image and its contrast was improved using the contrast limited adaptive histogram equalization method, as it provides various adjusting parameters to enhance the image. Afterwards, the obtained image was split into 28 parts. Then, each divided image was employed with a modified watershed technique. The inbuilt ‘regionprop’ function of MATLAB was used to calculate bubble characteristics.

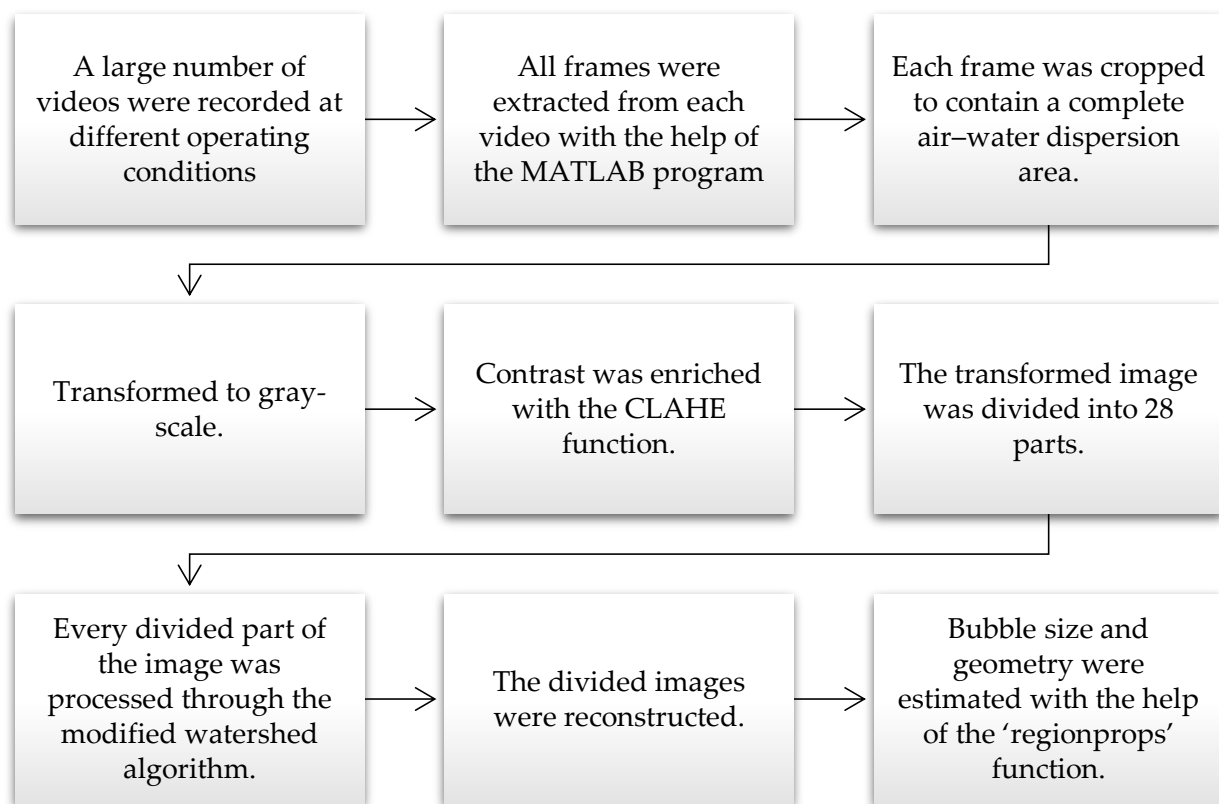


**Figure 4.** Steps for the IP algorithm applied for estimation of bubble characteristics.

### 3. Results

With the visual examination of the reactor, the existence of a foam region was observed at the top. Some bubbles exploded at the top, escaping the air–water dispersion area, which resulted in the entrainment of water above the gas–liquid dispersion. It was difficult to estimate the value of  $W_f$  manually due to the rapid variation of gas–liquid dispersion height. Even more challenging was identifying the entry region. This is because in the entry region, there are many bubbles with small diameter, covering the maximum area.

#### 3.1. Pixel Intensity in Vertical Direction

A grayscale image of the complete bubbling bed is presented in Figure 5a. After applying an image processing technique, the reconstructed image is presented in Figure 5b. The deviation of PI with height above the gas distributor for  $U$  equals  $0.105 \text{ ms}^{-1}$  and  $H_c$  equals  $0.145 \text{ m}$  (corresponding to Figure 5a), as presented in Figure 5c. The lower portion

of the bi-level image shows the region close to the gas distributor. At 0.37 m height, a low PI was observed. It appears due to the entrainment of water after bursting of the bubble. The top layer of the air–water dispersion was uneven. The height at which the last peak was observed was considered as the value of  $H_e$  in every image.

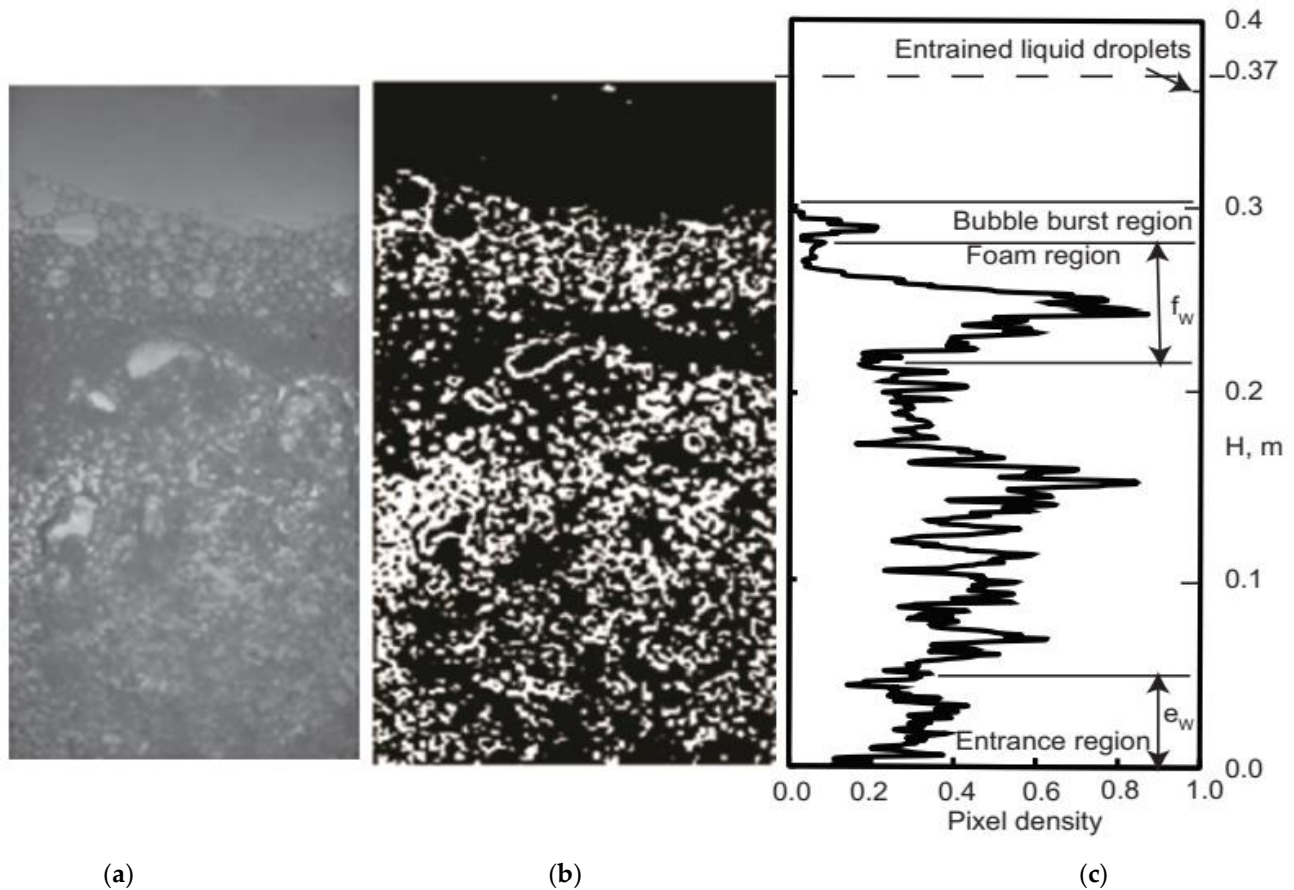


**Figure 5.** Image of gas–liquid dispersion in BC; (a) original image, (b) final bi-level image, (c) PI at different positions above the gas sparger.

The deviation of PI with height is not smooth. It exhibited a rising profile above the gas distributor. In most cases, a noticeable drop in PI was observed at a height equal to 0.04 m above the gas distributor. On visual observation, it was considered as the width of the entry region. PI exhibited a rising profile with increasing height. At about 0.22 m height above the gas distributor, there was a sudden drop in PI. It was again enhanced, increased to its maxima, and then dropped. It was noticed in all the experiments, which corresponded to the existence of a foam region. Due to an increase in bubble coalescence, a foam layer formed at the top of the gas–liquid dispersion bed. During few experiments, a small peak occurred again. This occurrence was resultant of bursting of air bubbles and considered while predicting the value of  $H_e$ .

The deviation of PI with the height of the reactor at different values of  $H_c$  and various  $U$  is shown in Figure 6. The profile is in qualitative accordance with that shown in Figure 5 for the complete range of  $U$  considered during experiments. The rise in PI at the bottom of the reactor is gradual. The drop in PI at a height greater than 0.15 m became less sharp with the rise in  $U$ . Beyond the expanded gas–liquid dispersion height, i.e., at  $H > H_e$ , the PI reduced to a very small value, showing the absence of any bubbles. In the air–water dispersion area below the foaming region, the maximum value of PI decreased with the increase in  $U$ .



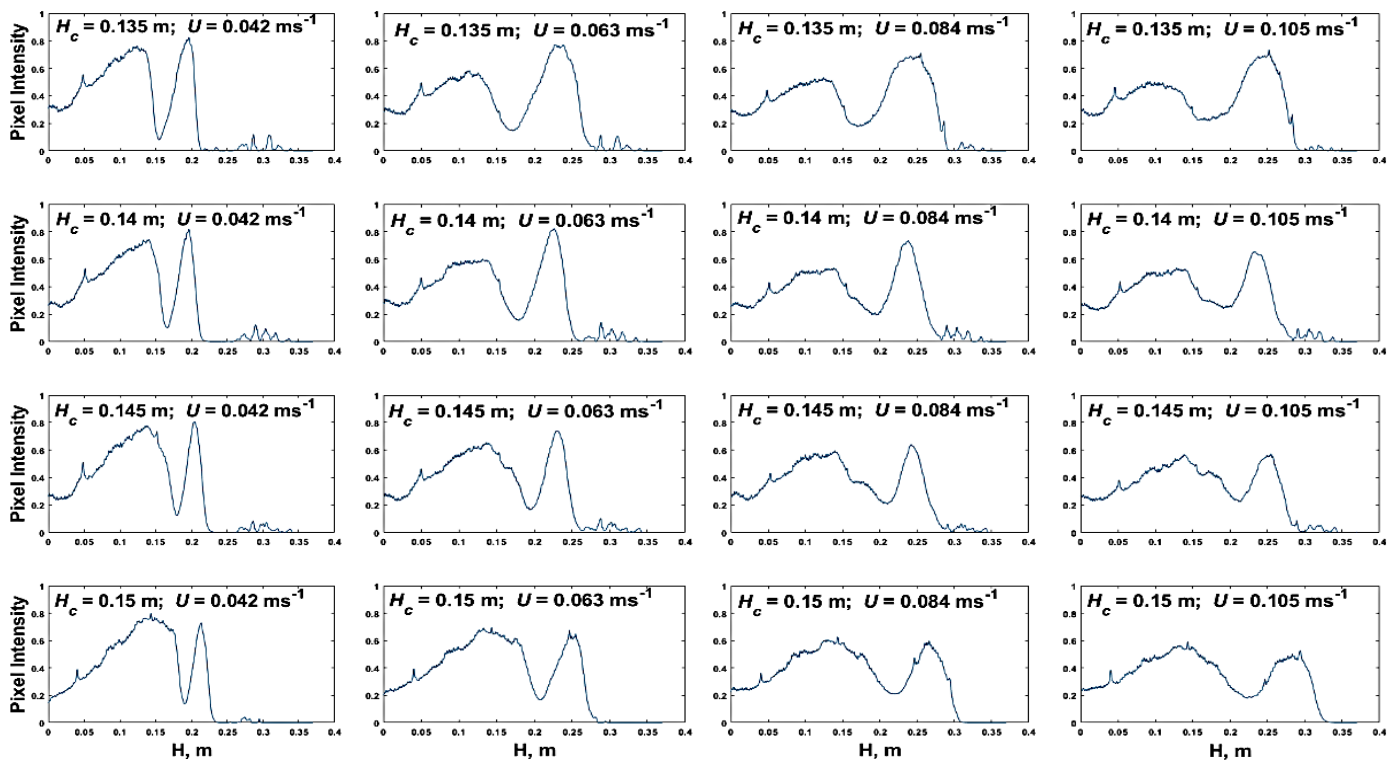


Figure 6. Variation of pixel intensity (axially) with  $U$  and  $H_c$ .

### 3.2. Foam Region Width

The value of  $W_f$  was calculated from graphs of PI vs. height. Variation of  $W_f$  with the  $U$  at  $H_c$  equal to 0.135 m is shown in Figure 7 and was compared with the models of refs. [6] and [7]. While using correlation (4),  $U$ , at which the inception of foaming takes place, was found by extrapolating data where  $W_f$  was equal to zero. The bubble size equal to 4 mm was estimated photographically.  $U_f$  thus calculated was equal to  $0.064 \text{ ms}^{-1}$ . Both expressions present monotonically rising data of  $W_f$ . When  $U = 0.042 \text{ ms}^{-1}$ , our data is in good agreement with the data estimated by both models of refs. [6] and [7]. Therefore, the approach proposed to estimate the value of  $W_f$  is verified.  $W_f$  calculated according to correlations 1 and 4 rose to 0.118 m and 0.132 m respectively at  $U = 0.168 \text{ ms}^{-1}$ . The maximum value of  $W_f$  was found to be equal to 0.061 m at  $U = 0.126 \text{ ms}^{-1}$ . This may be because the difference in bubble size corresponds to the variation of  $W_f$  at larger  $U$ .  $W_f$  was found as highly significant to bubble size [7].

The impact of  $U$  and  $H_c$  on  $W_f$  was investigated and is shown in Figure 8. The  $W_f$  was enhanced with rising  $U$  up to a value of  $U = 0.1 \text{ ms}^{-1}$ . On the further increase of  $U$ , the value of  $W_f$  reduced. This trend is similar for the complete range of  $H_c$  considered in this experimental study. The effect became less pronounced with the rise of clear liquid height. This profile is not in agreement with the results of ref. [6], who observed that the value of  $W_f$  was enhanced monotonically with rising  $U$ . The maximum  $W_f$  dropped with increasing  $H_c$ . The value of  $H_c$  taken in the current study was half the value taken by ref. [6]. This suggests that value of  $W_f$  may not obey the monotonic rising profile at small  $H_c$ .

The  $U$  at which the value of maximum  $W_f$  exists is equal to velocity up to which uniform bubbling takes place, i.e., up to  $U$  less than  $0.1 \text{ ms}^{-1}$ . When the uniform bubbling flow pattern shifted to a CT flow pattern, the value of  $W_f$  dropped. The proposed study did not include a large span of the CT flow regime. Small bubbles exist at low  $U$ ; therefore, bubble coalescence does not occur and bubbles exit from the reactor before it takes place. At high  $U$ , bubble coalescence occurs. It corresponds to the development of large bubbles which travel at high speed and get explode at top, escaping the air–water dispersion area.

Due to this, the value of  $W_f$  reduced. The present study was conducted at a low  $H_c$ . Hence, the proposed profile is appropriate for shallow beds only.

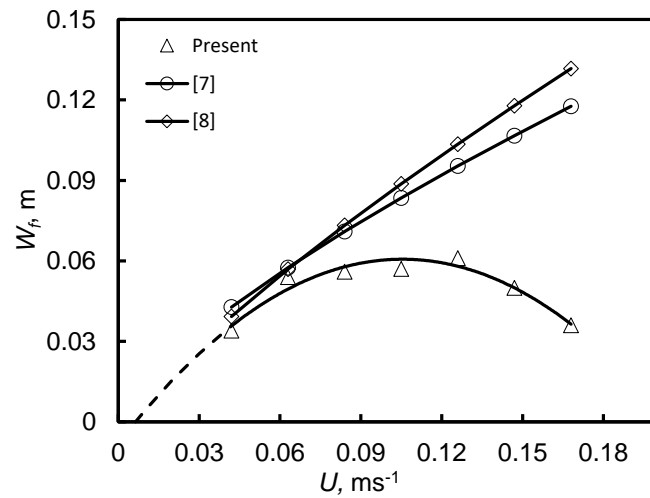


Figure 7. Comparison of  $W_f$  with the models available in the literature.

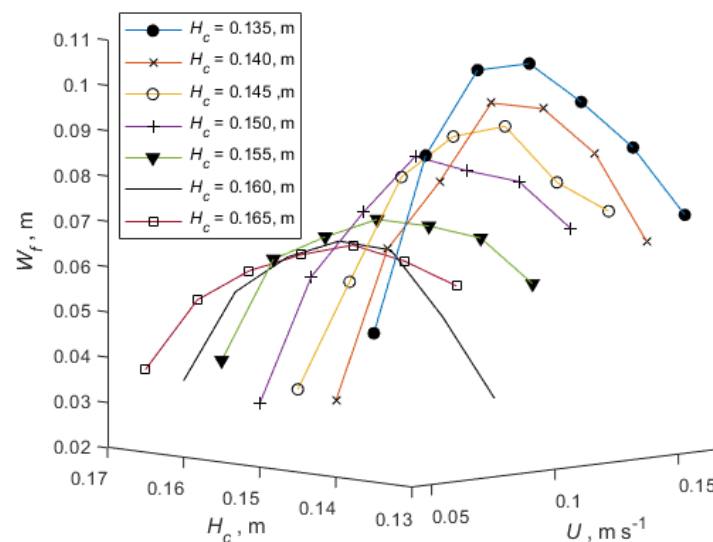


Figure 8. Variation of  $W_f$  with  $U$  and  $H_c$ .

### 3.3. Entry Region Width

The impact of  $H_c$  and  $U$  on  $W_e$  was investigated and is shown in Figure 9. The  $W_e$  was directly proportional to the value of  $H_c$ . It increased up to  $U = 0.084 \text{ ms}^{-1}$ . On the further increase of  $U$ , at low  $H_c$ ,  $W_e$  did not change. It dropped at high  $U$ . The profile is similar for the complete range of  $H_c$  considered in this experimental study. The present profile does not obey the monotonic rise of the entry region as estimated by correlation (3).

### 3.4. Gas Holdup

Experimental values of gas holdup were calculated according to correlation (10).

$$\varepsilon = \frac{(H_e - H_c)}{H_e} \tag{10}$$

where  $H_e$  is the average expanded gas–liquid dispersion height. Gas holdup was also estimated according to PI of the bi-level image according to expression (11).

$$\varepsilon_{pixel} = \frac{\text{pixels occupied by bubbles}}{\text{total pixels}} \tag{11}$$

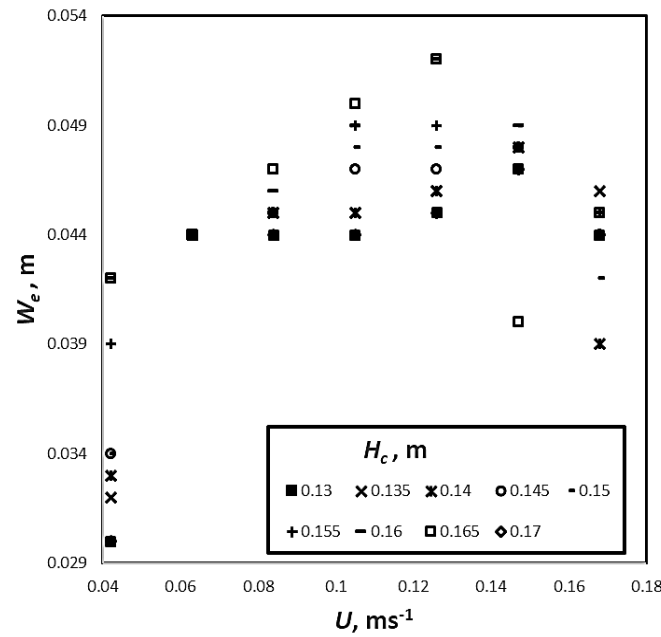


Figure 9. Variation of  $W_e$  with  $U$  and  $H_c$ .

An agreement between gas holdup calibrated according to the height estimation method and the PI method is shown in Figure 10a. At low gas holdup, data obtained from both methods were in good agreement. It recognizes the absence of a cluster of bubbles, or a very small number of bubble clusters were present. At large  $U$ , gas holdup increased, making the number of bubble clusters considerable. Consequently,  $\epsilon_{pixel}$  was less than  $\epsilon$ . When bubble clusters exist, the error is below 10%.

From bi-level images,  $\epsilon_{pixel}$  was calculated. Then to calculate  $\epsilon$ ,  $\epsilon_{pixel}$  was adjusted according to the correlation coefficient. Variation of  $\epsilon$  with  $U$  and  $H_c$  is shown in Figure 10b.

The  $\epsilon$  is directly proportional to  $U$ . The rise is intense at low  $U$ . When  $U$  is higher than transition velocity ( $U \approx 0.1 \text{ ms}^{-1}$ ), then bubble coalescence occurs and consequently the  $\epsilon$  rise is not as intense.  $\epsilon$  was much larger than that calculated in the literature. It recognizes the existence of a significant foam region.

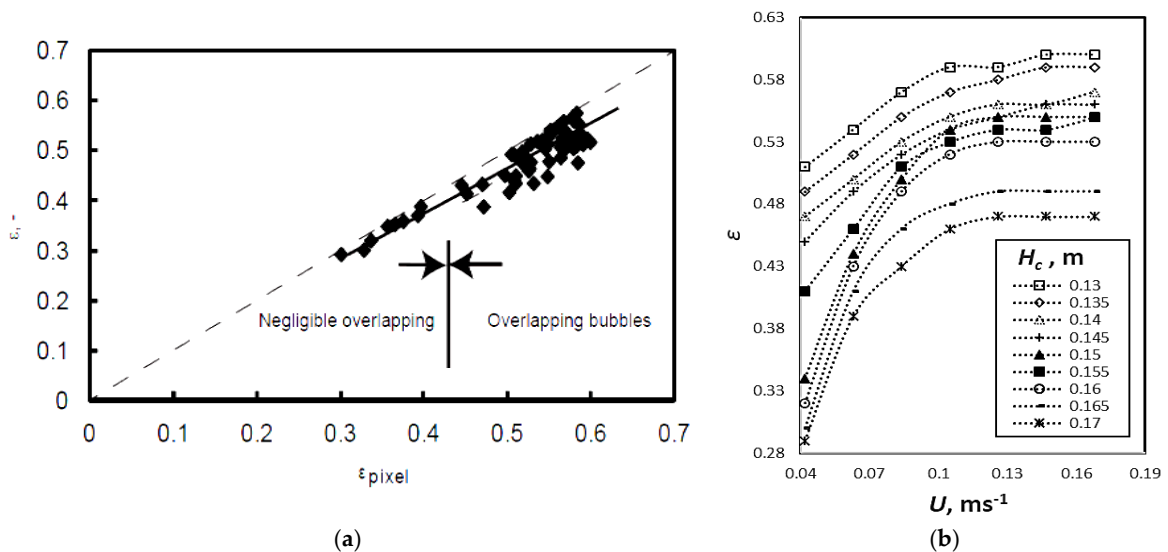


Figure 10. (a) Comparison between gas holdup measured by height estimation method and PI method. (b) Variation of  $\epsilon$  with  $U$  and  $H_c$ .

### 3.5. Bubble Size Distribution

The BSD at  $U = 0.0292 \text{ ms}^{-1}$  and  $H_c$  equal to 0.24 m is shown in Figure 11. It was challenging to identify very small bubbles ( $d_b < 0.002 \text{ m}$ ). It is worth noting that  $N_b$  reduced smoothly with the rise in bubble diameter. It was noticed that most bubbles were 2 mm to 6 mm in size. This flow pattern can be described as a transition to a CT flow pattern.

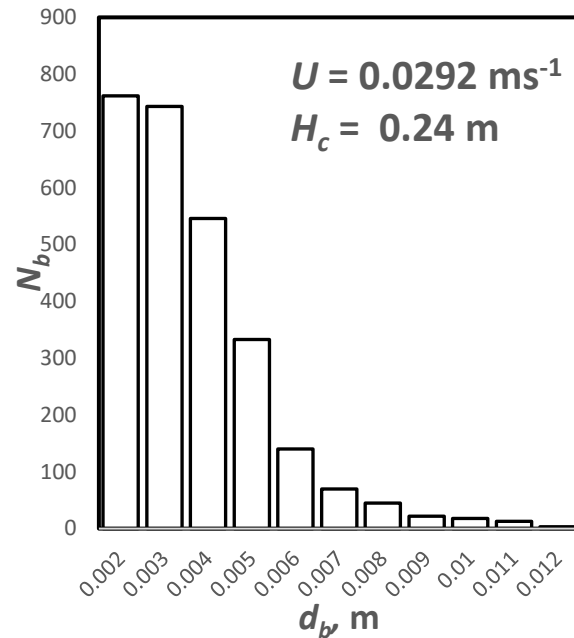


Figure 11. BSD at  $U = 0.0292 \text{ ms}^{-1}$  and  $H_c = 0.24 \text{ m}$ .

#### 3.5.1. Effect of $U$ on BSD

The variation of BSD with  $U$  is shown in Figure 12. It was noticed that the bubbles were of non-uniform size. It is worth noting that there was no significant effect of  $U$  on BSD.  $N_b$  was high for  $d_b$  equal to 2 mm.  $N_b$  smoothly reduced with the rise in bubble size. The highest value of  $N_b$  at  $d_b$  equal to 2 mm reduced with the rise in  $U$ .

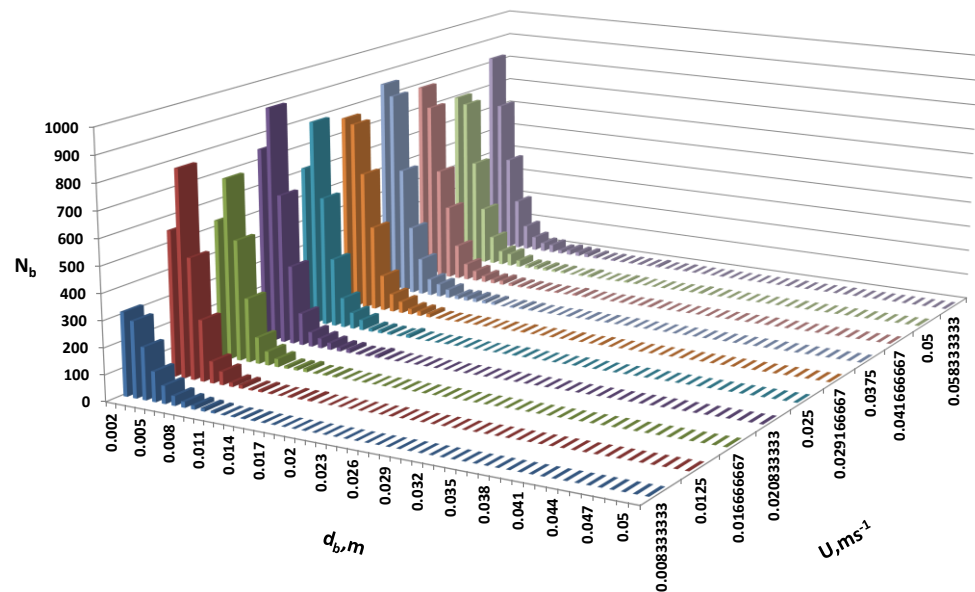


Figure 12. Variation of BSD with  $U$  at  $H_c = 0.24 \text{ m}$ .

### 3.5.2. Effect of $H_c$ on BSD

The BSD at  $U = 0.025 \text{ ms}^{-1}$  for different values of  $H_c$  (0.20–0.28 m) is shown in Figure 13. The BSD did not vary for the complete range of  $H_c$  considered in the present experiments.  $N_b$  for small bubbles was observed to increase slightly with the rise in  $H_c$ . It can be concluded that the effect of  $H_c$  on BSD is not significant.

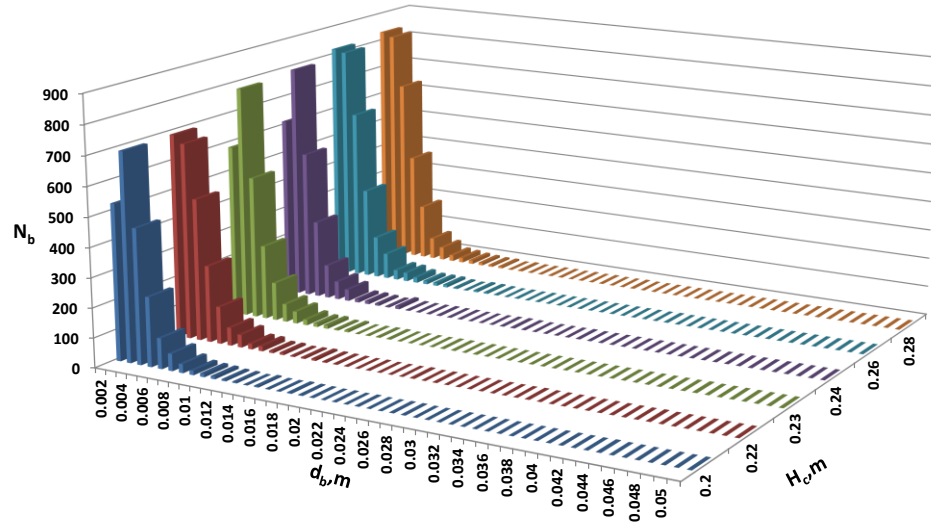


Figure 13. Variation of BSD with  $H_c$  at  $U = 0.025 \text{ ms}^{-1}$ .

### 3.6. Sauter-mean Bubble Diameter

From BSD, the value of Sauter mean bubble diameter was calculated by

$$d_{32} = \frac{\sum_i d_i^3}{\sum_i d_i^2} \tag{12}$$

where  $d_i$  is the projected area equivalent diameter of a single bubble.

Variation of  $d_{32}$  as a function of  $U$  and  $H_c$  is presented in Figure 14. The values of  $d_{32}$  seem to be independent of  $H_c$ . Sauter mean diameter increased with increasing  $U$ . There was little increase for  $U < 0.04 \text{ ms}^{-1}$ . Above this value of  $U$  there was a significant increase in  $d_{32}$ . It can be concluded that above  $U = 0.04 \text{ ms}^{-1}$ , bubble coalescence occurs.

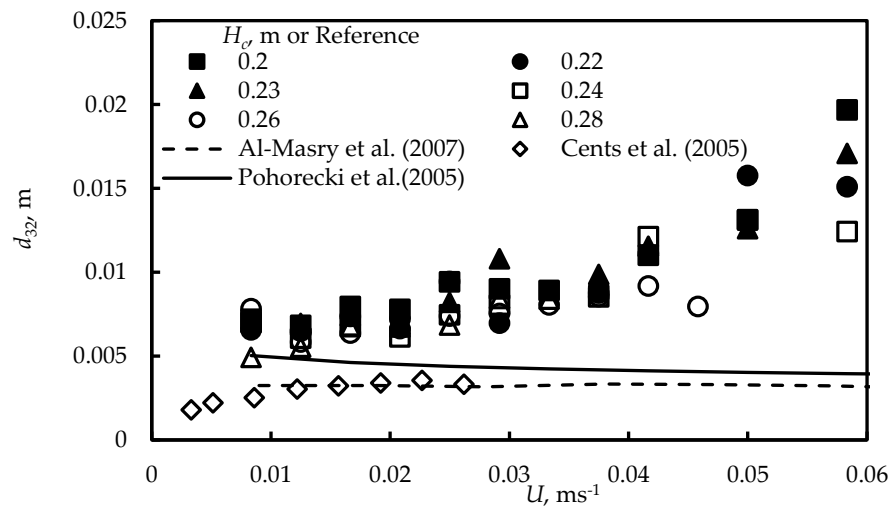


Figure 14. Variation of  $d_{32}$  as a function of  $U$  and  $H_c$ .

Data of ref. [33] also show that  $d_{32}$  increases with increasing  $U$ ; however, the present data are about 100% higher than their data, due to the use of a sintered porous plate as the

gas distributor. Therefore, the size of bubbles formed at the sparger in their studies could have been lower than that formed in the present studies.

Ref. [35] carried out numerical experiments and proposed the following equation for  $d_{32}$  after validating the equation for seven organic solvents.

$$d_{32} = 0.289\rho^{-0.552}\mu^{-0.048}\sigma^{0.442}U_g^{-0.124} \quad (13)$$

Present values were compared with those predicted using Equation (13) and presented in Figure 14. The predicted values of  $d_{32}$  were lower than the present experimental values of  $d_{32}$ . Equation (13) predicts bubble size to decrease with increasing  $U$ . Similar trends were also discussed in literature by refs. [17,36]. This trend is contrary to the present trend.

The experimental results of ref. [37] are also presented in Figure 14. These values are also lower than the present values. This may be because the hole diameter in the sparger in their study was 0.001 m, which is lower than that used in the present study. If the bubble coalescence or breakup phenomenon does not take place, then the bubble diameter in the column will be approximately equal to that formed at the gas distributor.

#### 4. Conclusions

This research concerned the identification of different gas–liquid dispersion zones and the measurement of gas holdup, BSD, and Sauter mean bubble diameter. A non-invasive method, i.e., an image analysis technique, was proposed for determining different bed zones and hydrodynamic parameters of the bubble column. The results were analyzed, and it can be concluded that  $W_f$  showed maxima at  $U = 0.1 \text{ ms}^{-1}$  and was less noticeable at large  $H_c$ .  $W_e$  also showed a maximum at  $U = 0.1 \text{ ms}^{-1}$ . It was directly proportional to  $H_c$ . The foaming region and the region near the gas distributor had an opposite behavior with respect to  $H_c$ .  $\varepsilon_{pixel}$  deviated slightly from  $\varepsilon$  with the rise in  $U$ .  $\varepsilon_{pixel}$  were corrected to obtain  $\varepsilon$ . Gas holdup was directly proportional to  $U$  at a given value of  $H_c$ .  $\varepsilon$  was indirectly proportional to  $H_c$ .  $N_b$  was high for  $d_b$  equal to 2 mm.  $N_b$  smoothly reduced with the rise in bubble size. The highest value of  $N_b$  at  $d_b$  equal to 2 mm reduced with the rise in  $U$ . The number of small bubbles seemed to increase slightly with increasing  $H_c$ . The values of Sauter mean bubble diameter increased with increasing  $U$ . There was little increase for  $U < 0.04 \text{ ms}^{-1}$ . Above this value of  $U$  there was a significant increase in  $d_{32}$ . It can be concluded that above  $U = 0.04 \text{ ms}^{-1}$ , bubble coalescence occurs. The increase was greater in the churn turbulent regime. Data of ref. [33] also showed that  $d_{32}$  increases with increasing  $U$ ; however, the present data are about 100% higher than their data due to the use of a sintered porous plate as the gas distributor. Therefore, the size of bubbles formed at the sparger in their studies could have been lower than that formed in the present studies.

**Author Contributions:** N.A.: Conceptualization, data curation, formal analysis, investigation, methodology, software, validation, visualization, writing—original draft, writing—review and editing. H.K.: Conceptualization, writing—review and editing, funding acquisition, resources. M.L.: Conceptualization, writing—review and editing. All authors have read and agreed to the published version of the manuscript.

**Funding:** This work was supported by Basic Science Research Program through the National Research Foundation of Korea (NRF) funded by the Ministry of Education (NRF-2017R1D1A1B04032598). This work was supported by the 2021 Yeungnam University Research Grant.

**Institutional Review Board Statement:** Not applicable.

**Informed Consent Statement:** Not applicable.

**Data Availability Statement:** Not applicable.

**Conflicts of Interest:** The authors declare no conflict of interest.

## Nomenclature

$a_a$	aerated area containing all holes
$a_c$	cross-sectional area
AR	aspect ratio
BC	bubble column
BSD	bubble size distribution
$Bo$	Bond number
$Ca$	Capillary number
CT	churn turbulent
$d_{32}$	Sauter mean bubble diameter
$d_b$	diameter of bubbles
D	Column diameter, m
$d_o$	Sparger hole diameter, m
$Fr$	Froude number
$Ga$	Galileo number
$H_c$	clear liquid height
$H_e$	average expanded gas-liquid dispersion height
IP	image processing
$N_b$	number of bubbles
PI	pixel intensity
PP	perforated plate
$Re$	Reynolds number
SN	single nozzle
$U$	superficial gas velocity
$U_f$	superficial gas velocity at inception of foaming
$U_t$	terminal rise velocity
$W_e$	entry region thickness
$W_f$	foam region thickness
$\mu_l$	viscosity of liquid phase
$\rho_l$	density of liquid phase
$\sigma_l$	surface tension of liquid phase
$\epsilon$	gas holdup
$\epsilon_{pixel}$	gas holdup estimated according to pixel intensity

## References

- Paul, T.; Sinharoy, A.; Pakshirajan, K.; Pugazhenthii, G. Lipid-rich Bacterial Biomass Production Using Refinery Wastewater in a Bubble Column Bioreactor for Bio-Oil Conversion by Hydrothermal Liquefaction. *J. Water Process Eng.* **2020**, *37*, 101462. [[CrossRef](#)]
- Verma, A.K. *Process Modeling and Simulation in Chemical, Biochemical and Environmental Engineering*, 1st ed.; CRC Press: Boca Raton, FL, USA, 2014; ISBN 9780429090691.
- Mohan, T.R.; Kumar, M.S.M.; Rao, L. Numerical Modelling of Oxygen Mass Transfer in Diffused Aeration Systems: A CFD-PBM Approach. *J. Water Process Eng.* **2021**, *40*, 101920. [[CrossRef](#)]
- Bennett, M.A.; West, R.M.; Luke, S.P.; Williams, R.A. The Investigation of Bubble Column and Foam Processes Using Electrical Capacitance Tomography. *Miner. Eng.* **2002**, *15*, 225–234. [[CrossRef](#)]
- Veera, U.; Kataria, K.; Joshi, J. Effect of Superficial Gas Velocity on Gas Hold-Up Profiles in Foaming Liquids in Bubble Column Reactors. *Chem. Eng. J.* **2004**, *99*, 53–58. [[CrossRef](#)]
- Yamashita, F. Effect of foam layer on gas holdup in a bubble column. *J. Chem. Eng. Japan* **1995**, *28*, 837–840. [[CrossRef](#)]
- Pilon, L.; Fedorov, A.G.; Viskanta, R. Steady-State Thickness of Liquid–Gas Foams. *J. Colloid Interface Sci.* **2001**, *242*, 425–436. [[CrossRef](#)]
- Amirnia, S.; de Bruyn, J.R.; Bergougnou, M.A.; Margaritis, A. Continuous Rise Velocity of Air Bubbles in Non-Newtonian Biopolymer Solutions. *Chem. Eng. Sci.* **2013**, *94*, 60–68. [[CrossRef](#)]
- Zaruba, A.; Krepper, E.; Prasser, H.-M.; Schleicher, E. Measurement of Bubble Velocity Profiles and Turbulent Diffusion Coefficients of the Gaseous Phase in Rectangular Bubble Column Using Image Processing. *Exp. Therm. Fluid Sci.* **2005**, *29*, 851–860. [[CrossRef](#)]
- Lau, Y.M.; Sujatha, K.T.; Gaeini, M.; Deen, N.G.; Kuipers, J.A.M. Experimental Study of the Bubble Size Distribution in a Pseudo-2D Bubble Column. *Chem. Eng. Sci.* **2013**, *98*, 203–211. [[CrossRef](#)]
- Lau, Y.M.; Deen, N.G.; Kuipers, J.A.M. Development of an Image Measurement Technique for Size Distribution in Dense Bubbly Flows. *Chem. Eng. Sci.* **2013**, *94*, 20–29. [[CrossRef](#)]

12. Fu, Y.; Liu, Y. Development of a Robust Image Processing Technique for Bubbly Flow Measurement in a Narrow Rectangular Channel. *Int. J. Multiph. Flow* **2016**, *84*, 217–228. [[CrossRef](#)]
13. Zhong, S.; Zou, X.; Zhang, Z.; Tian, H. A Flexible Image Analysis Method for Measuring Bubble Parameters. *Chem. Eng. Sci.* **2016**, *141*, 143–153. [[CrossRef](#)]
14. Ahmed, F.S.; Sensenich, B.A.; Ghenni, S.A.; Znerdstrovic, D.; Al-Dahhan, M.H. Bubble Dynamics in 2D Bubble Column: Comparison between High-Speed Camera Imaging Analysis and 4-Point Optical Probe. *Chem. Eng. Commun.* **2015**, *202*, 85–95. [[CrossRef](#)]
15. Besagni, G.; Inzoli, F. Bubble size Distributions and Shapes in Annular Gap Bubble Column. *Exp. Therm. Fluid Sci.* **2016**, *74*, 27–48. [[CrossRef](#)]
16. Besagni, G.; Inzoli, F. Comprehensive Experimental Investigation of Counter-Current Bubble Column Hydrodynamics: Holdup, Flow Regime Transition, Bubble Size Distributions and Local Flow Properties. *Chem. Eng. Sci.* **2016**, *146*, 259–290. [[CrossRef](#)]
17. Akita, K.; Yoshida, F. Bubble Size, Interfacial Area, and Liquid-Phase Mass Transfer Coefficient in Bubble Columns. *Ind. Eng. Chem. Process Des. Dev.* **1974**, *13*, 84–91. [[CrossRef](#)]
18. Kumar, A.; Degaleesan, T.E.; Laddha, G.S.; Hoelscher, H.E. Bubble Swarm Characteristics in Bubble Columns. *Can. J. Chem. Eng.* **1976**, *54*, 503–508. [[CrossRef](#)]
19. Gaddis, E.; Vogelpohl, A. Bubble Formation in Quiescent Liquids under Constant Flow Conditions. *Chem. Eng. Sci.* **1986**, *41*, 97–105. [[CrossRef](#)]
20. Walter, J.F.; Blanch, H.W. Liquid Circulation Patterns and Their Effect on Gas Hold-Up and Axial Mixing in Bubble Columns. *Chem. Eng. Commun.* **1983**, *19*, 243–262. [[CrossRef](#)]
21. Pohorecki, R.; Moniuk, W.; Bielski, P.; Sobieszuk, P. Diameter of Bubbles in Bubble Column Reactors Operating with Organic Liquids. *Chem. Eng. Res. Des.* **2005**, *83*, 827–832. [[CrossRef](#)]
22. Jamialahmadi, M.; Zehtaban, M.R.; Müller-Steinhagen, H.; Sarrafi, A.; Smith, J.M. Study of Bubble Formation under Constant Flow Conditions. *Chem. Eng. Res. Des.* **2001**, *79*, 523–532. [[CrossRef](#)]
23. Pohorecki, R.; Moniuk, W.; Bielski, P.; Zdrójkowski, A. Modelling of the Coalescence/Redispersion Processes in Bubble Columns. *Chem. Eng. Sci.* **2001**, *56*, 6157–6164. [[CrossRef](#)]
24. Jamshidi, N.; Mostoufi, N. Investigating Bubble Dynamics in a Bubble Column Containing Shear Thinning Liquid Using a Dual-Tip Probe. *Exp. Therm. Fluid Sci.* **2018**, *94*, 34–48. [[CrossRef](#)]
25. Kanaris, A.G.; Pavlidis, T.I.; Chatzidafni, A.P.; Mouza, A.A. The Effects of the Properties of Gases on the Design of Bubble Columns Equipped with a Fine Pore Sparger. *ChemEngineering* **2018**, *2*, 11. [[CrossRef](#)]
26. Mouza, A.A. Design of Bubble Columns Equipped with Porous Sparger. *Mater. Today Proc.* **2018**, *5*, 27572–27581. [[CrossRef](#)]
27. Azizi, S.; Yadav, A.; Lau, Y.M.; Hampel, U.; Roy, S.; Schubert, M. Hydrodynamic Correlations for Bubble Columns from Complementary UXCT and RPT Measurements in Identical Geometries and Conditions. *Chem. Eng. Sci.* **2019**, *208*, 115099. [[CrossRef](#)]
28. Feng, D.; Ferrasse, J.-H.; Soric, A.; Boutin, O. Bubble Characterization and Gas–Liquid Interfacial Area in Two Phase Gas–Liquid System in Bubble Column at Low Reynolds Number and High Temperature and Pressure. *Chem. Eng. Res. Des.* **2019**, *144*, 95–106. [[CrossRef](#)]
29. Cordero, J.R.V.; Sámano, D.; Zenit, R. Study of the Properties of Bubbly Flows in Boger-Type Fluids. *J. Non-Newton. Fluid Mech.* **2012**, *175–176*, 1–9. [[CrossRef](#)]
30. Karn, A.; Ellis, C.; Arndt, R.; Hong, J. An Integrative Image Measurement Technique for Dense Bubbly Flows with a Wide Size Distribution. *Chem. Eng. Sci.* **2015**, *122*, 240–249. [[CrossRef](#)]
31. Guan, X.; Yang, N. Bubble Properties Measurement in Bubble Columns: From Homogeneous to Heterogeneous Regime. *Chem. Eng. Res. Des.* **2017**, *127*, 103–112. [[CrossRef](#)]
32. Lau, Y.M.; Möller, F.; Hampel, U.; Schubert, M. Ultrafast X-ray Tomographic Imaging of Multiphase Flow in Bubble Columns—Part 2: Characterisation of Bubbles in the Dense Regime. *Int. J. Multiph. Flow* **2018**, *104*, 272–285. [[CrossRef](#)]
33. Cents, A.H.G.; Jansen, D.J.W.; Brilman, D.W.F.; Versteeg, G.F. Influence of small amounts of additives on gas hold-up, bubble size, and interfacial area. *Ind. Eng. Chem. Res.* **2005**, *44*, 4863–4870. [[CrossRef](#)]
34. Cui, Y.; Li, C.; Zhang, W.; Ning, X.; Shi, X.; Gao, J.; Lan, X. A Deep Learning-Based Image Processing Method for Bubble Detection, Segmentation, and Shape Reconstruction in High Gas Holdup Sub-Millimeter Bubbly Flows. *Chem. Eng. J.* **2022**, *449*, 137859. [[CrossRef](#)]
35. Pohorecki, R.; Moniuk, W.; Zdrójkowski, A. Hydrodynamics of a Bubble Column under Elevated Pressure. *Chem. Eng. Sci.* **1999**, *54*, 5187–5193. [[CrossRef](#)]
36. Millies, M.; Mewes, D. Interfacial Area Density in Bubbly Flow. *Chem. Eng. Process. Process Intensif.* **1999**, *38*, 307–319. [[CrossRef](#)]
37. Al-Masry, W.A.; Ali, E.M.; Aqeel, Y.M. Effect of Antifoam Agents on Bubble Characteristics in Bubble Columns Based on Acoustic Sound Measurements. *Chem. Eng. Sci.* **2006**, *61*, 3610–3622. [[CrossRef](#)]